SECTION III. TASK 3. COMPREHENSIVE MODEL DEVELOPMENT AND EVALUATION

Objectives

The objective of this task is to integrate advanced chemistry and physics submodels into a comprehensive two-dimensional model of entrained-flow reactors (PCGC-2) and to evaluate the model by comparing with data from well-documented experiments. Approaches for the comprehensive modeling of fixed-bed reactors will also be reviewed and evaluated and an initial framework for a comprehensive fixed-bed code will be employed after submission of a detailed test plan (Subtask 3.b).

Task Outline

This task is being performed in three subtasks. The first covers the full 60 months of the program and is devoted to the development of the entrained-bed code. The second subtask is for fixed-bed reactors and is divided into two parts. The first part (12 months) was devoted to reviewing the state-of-the-art in fixed-bed reactors. This led to the development of the research plan for fixed-bed reactors, which was approved. The code development is being done in the remaining 45 months of the program. The third subtask is to generalize the entrained-bed code to fuels other than dry pulverized coal and will be performed during the last 24 months of the program.

III.A. SUBTASK 3.A. - INTEGRATION OF ADVANCED SUBMODELS INTO ENTRAINED-FLOW CODE, WITH EVALUATION AND DOCUMENTATION

Senior Investigators - B. Scott Brewster and L. Douglas Smoot
Brigham Young University
Provo, UT 84602
(801) 378-6240 and 4326

Research Assistant - Susana K. Berrondo

Objectives

The objectives of this subtask are 1) to integrate the FG-DVC submodel into PCGC-2, 2) incorporate additional submodels and improvements developed under Task 2, 3) validate the improved code, 4) improve user-friendliness and robustness, and 5) document the code.

Accomplishments

Work continued on modeling the transparent wall reactor for code validation and on developing a graphical, user-friendly interface. Accomplishments are described below.

Transparent Wall Reactor

Data are available for non-reacting flow and for three coal flames in the AFR transparent wall reactor. Reasonable results have been achieved for the simulation of the non-reacting flow case and the "fast-flow" Rosebud coal flame. These results were obtained by assuming a coal-carrier stream inlet diameter of 2 mm at the nozzle exit, consistent with visual observation.

Simulation Results - Temperature profiles at several axial locations are shown in Figure III.A-1 for gas flow without particles. The data were obtained with an unshielded thermocouple and subsequently corrected for heat loss. The inlet radial profile has a low-temperature core (coal carrier gas) surrounded by hot air which is surrounded by cold (room) air. As the gas progresses up the reactor, the core heats up by diffusion and convection induced by buoyancy, and the gradient between the hot air and room air becomes less steep. Finally, a point is reached where the depression in the core disappears entirely, and the profile become peaked at the center. The

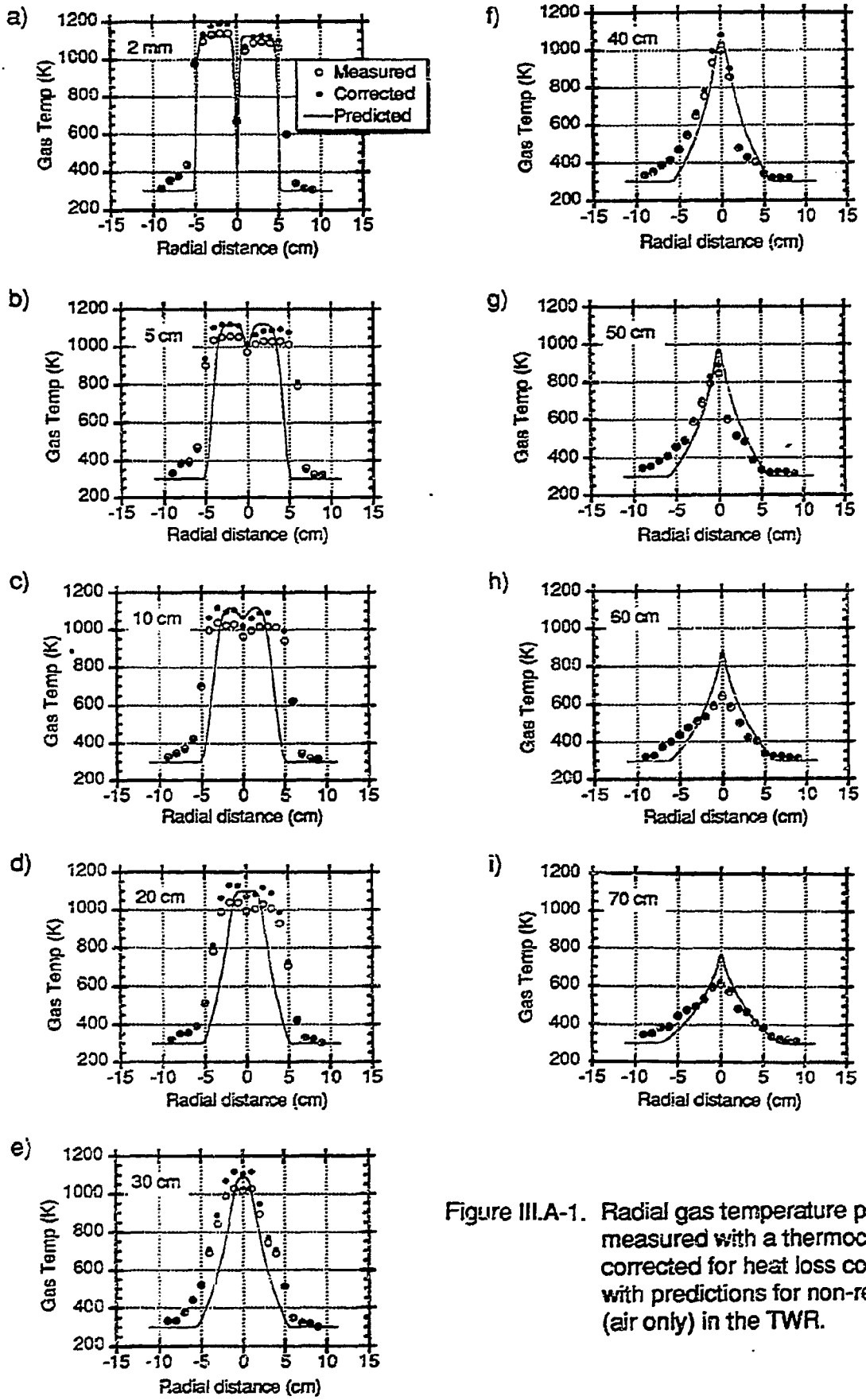

Figure III.A-1. Radial gas temperature profile data measured with a thermocouple and corrected for heat loss compared with with predictions for non-reacting flow (air only) in the TWR.

peakedness is caused by the convection toward the centerline induced by buoyancy. Overall, the agreement with the data is quite good. The thermocouple measurements near the screen (2 mm) at a radius greater than 5 cm are too high, probably due to radiation from the hot screen, although the corrections don't seem to be much of an improvement. The mixing rate between the hot air and room air seems to be overpredicted. This could also be a result of overpredicting buoyancy forces. The transition from cold core to a peak at the centerline is accurately predicted.

Similar data for the coal flame are presented in Figure III.A-2. When particles are present, there is an immediate rise in temperature at the core following ignition. In this flame, ignition occurred at 10 cm. The peaked nature of the profile is enhanced by the more dominant buoyancy forces compared to the gas-only case, due to the higher temperature in the core caused by the flame. Again the overall prediction of trends in the shape of the profile seem to be predicted fairly well. Interestingly, the uncorrected thermocouple measurements seem to agree better with the predictions than the corrected values. Heat-loss corrections in coal flames are quite uncertain owing to the effects of gas and soot radiation in the flame and coating of the thermocouple with soot.

Computed particle trajectories are shown in Figure III.A-3. Figure III.A-3a shows the complete trajectories. Figure III.A-3b shows only the portion of each trajectory where the particle temperature exceeds 1000 K and the particle is not completely burned out. The particles ignite at from 5 to 9 cm above the exit of the nozzle. The particles near the outer edge of the stream ignite first, as expected, since they are the first to mix with the preheated air. They also react the most quickly and burn out first, causing the width of the glowing particle stream to reach a maximum and then taper in toward the center of the reactor. The width of the particle stream also undergoes a rapid expansion at the ignition point as hot gases generated by combustion suddenly force the particle stream outward.

Measured and predicted particle velocities are compared in Figure III.A-4. These measurements were obtained from the length of streaks recorded with a video camera. Calculations for two particle sizes and two starting locations are shown. The outer-edge particles accelerate more quickly than the centerline particles due to the sudden expansion of the gas as it enters the flow domain. The centerline particles don't accelerate until after ignition, at which time buoyancy forces and expansion due to heating cause the

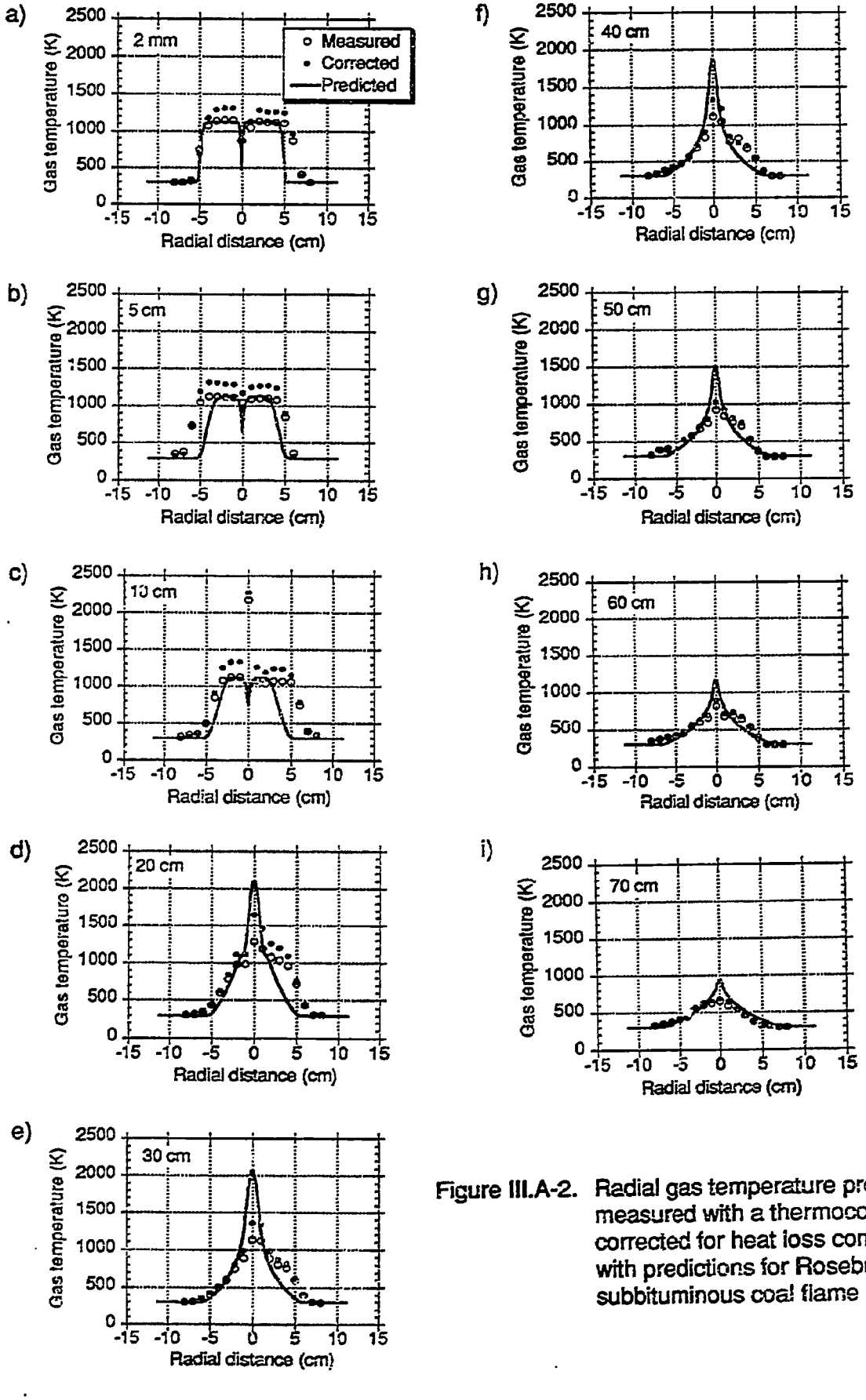

Figure III.A-2. Radial gas temperature profile data measured with a thermocouple and corrected for heat loss compared with with predictions for Rosebud subbituminous coal flame in the TWR.

a) Complete trajectories

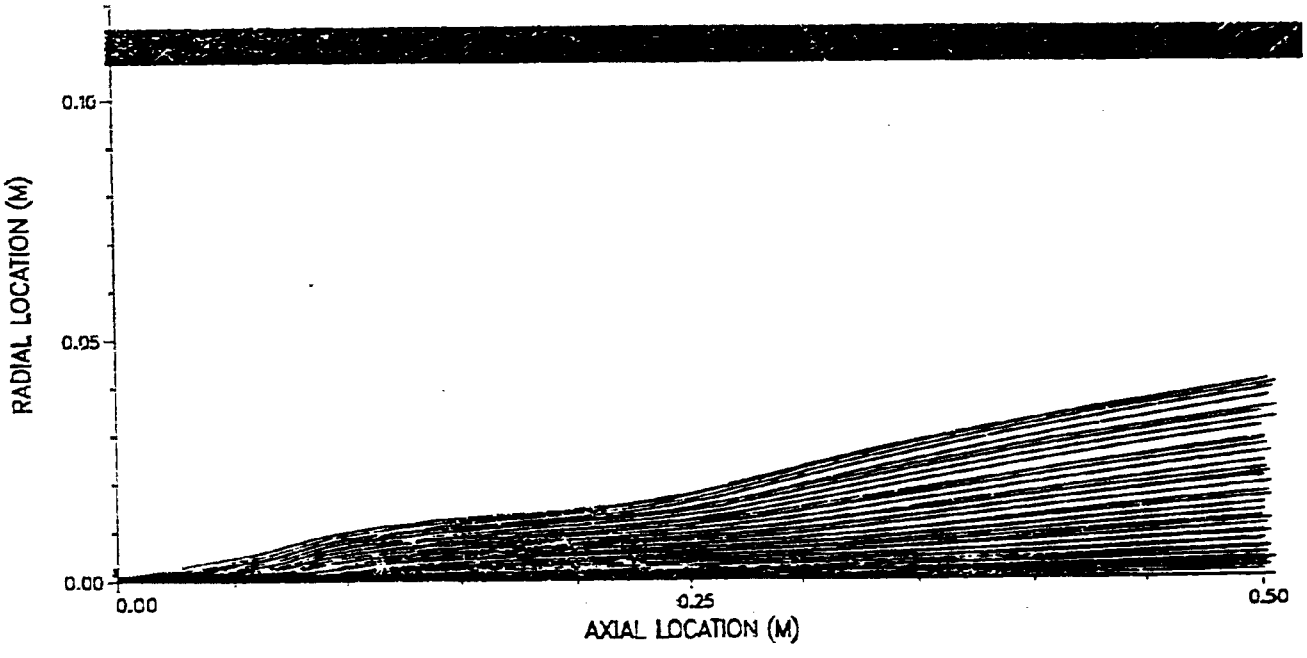

b) Trajectories of ignited particles

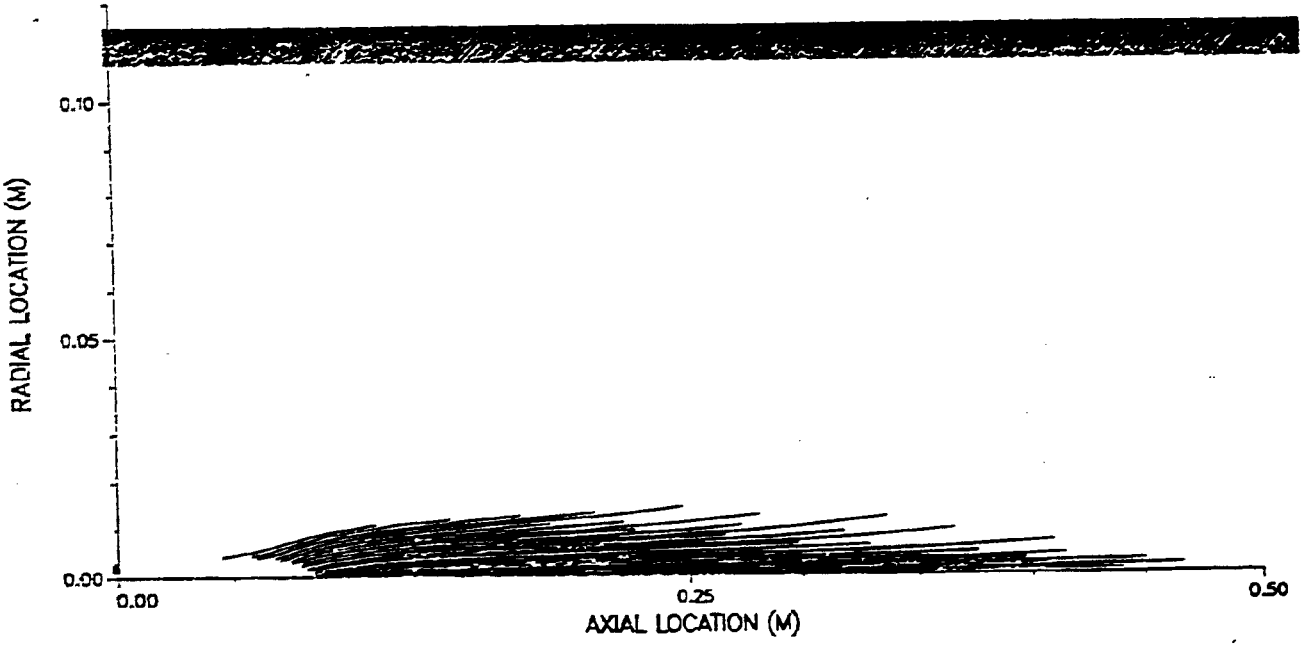

Figure III.A-3. Computed particle trajectories for Montana Rosebud coal flame in the TWR.

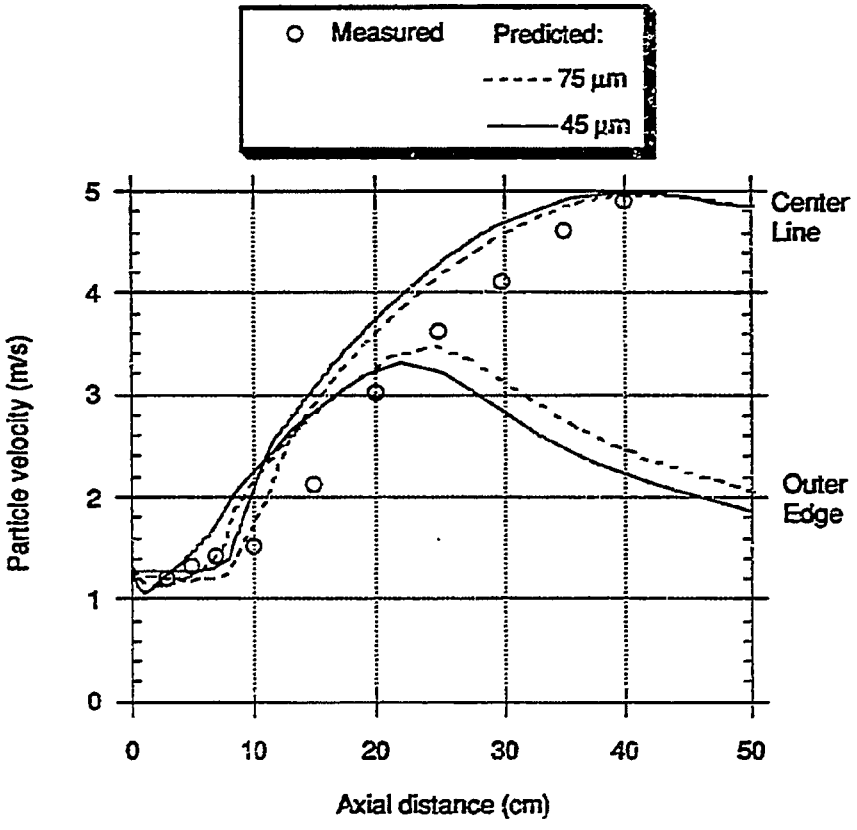

Figure III.A-4. Particle velocity determined from streaks on a video recording compared with predictions for 45 μm and 75 μm particles at the centerline and at the outer edge of the coal particle stream for a Rosebud subbituminous coal flame in the TWR.

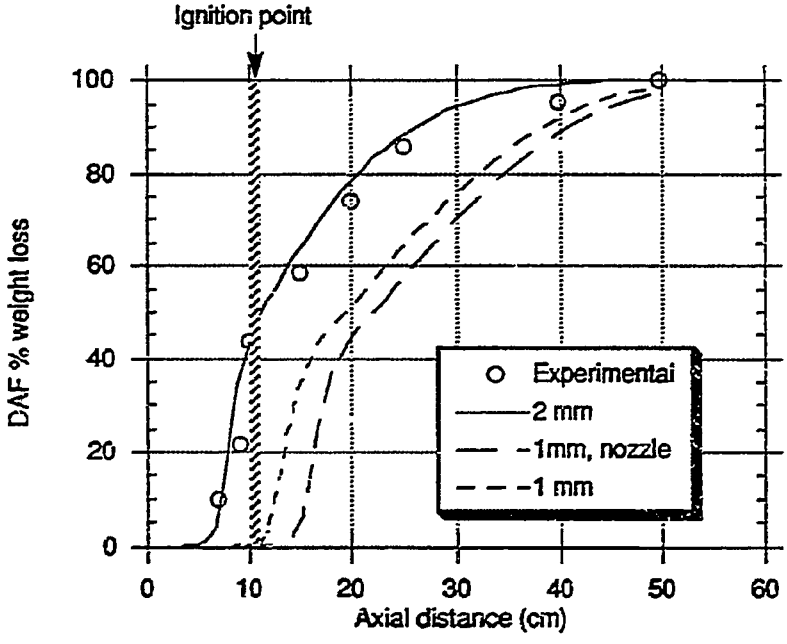

Figure III.A-5. Radially integrated particle burnout determined by the ash tracer method compared with predicted burnout for three cases for a Rosebud subbituminous coal flame in the TWR. The three cases are a 1- and 2-mm-diameter coal stream with the nozzle excluded from the calculational domain and a 1-mm-diameter coal stream with the nozzle included.

gas velocity to increase near the center of the reactor. The centerline particles continue to accelerate until the radial velocity profile begins to flatten due to the effects of diffusion. The outer edge particles, on the other hand, accelerate with the centerline particles, but then decelerate as they spread away from the centerline where the velocity is lower. These particles are, however, burned out (see Fig. III.A-3b) and so are not seen in the video recording. Predicted particle velocity is quite independent of particle size. It is also fairly independent of starting location in the pre- and early-flame regions, but then becomes a strong function of particle position. Predicted velocity exceeds the measured values up to the point where it becomes a strong function of particle position. The predicted velocity for the visible trajectories agrees fairly well with the measured values.

Particle burnout is shown in Figure III.A-5. Three cases are shown: a 1-mm-diameter coal stream at the nozzle exit (nozzle excluded from the calculational domain), a 2-mm-diameter coal stream at the nozzle exit, and 1-mm-diameter coal stream at the nozzle entrance (nozzle included in the calculational domain). The coal stream enters the reactor through a 1-mm-diameter tube, which expands into a 5-mm-diameter nozzle. As shown, the burnout curve is predicted very well for the inlet condition of a 2-mm-diameter coal stream at the nozzle exit, which is consistent with visual observation of the stream as it exits the nozzle. The curve is shifted to the right for the 1-mm case (nozzle excluded) because of the increased velocity. The 1-mm case with nozzle included was apparently unable to resolve the complex flow in the nozzle with the current grid spacing. Detailed simulation of the nozzle revealed the presence of recirculation zones which extended beyond the nozzle exit into the reactor. The slight "knee" in the curve at 40 percent burnout is due to the transition from devolatilization to heterogeneous oxidation of the residual char. The shape of the burnout curve is fairly insensitive to the assumed coal stream inlet diameter and particle velocity, but the curve (and ignition point) can be shifted several centimeters to the right or left by varying the particle inlet assumptions.

Tomography data and predictions are shown in Figs. III.A-6 to 8. Figure III.A-6 presents the particle and gas temperatures. A symbol is shown for the temperature of each particle trajectory as it crosses the indicated axial distance. At 6 cm, the particles are being heated by the gas and lag the gas temperature. At the edge of the particle stream, it appears that one of the smallest particles (45 μm) is ignited. Measurements indicate the presence of

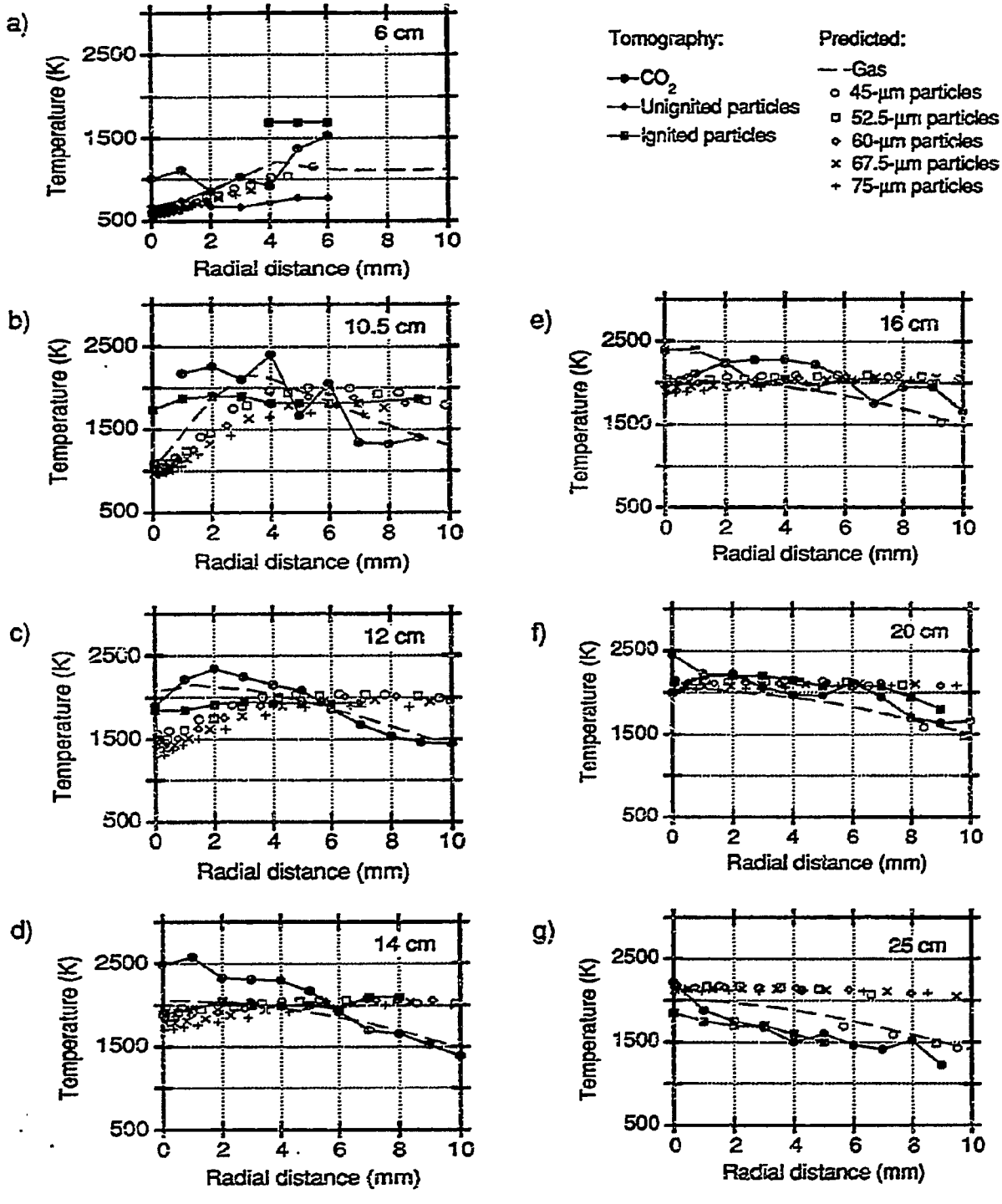

Figure III.A-6. Radial CO_2 and particle temperature profiles determined from tomographic reconstruction of FT-IR emission/transmission spectra compared with predicted gas and particle temperature for a Rosebud subbituminous coal flame in the TWR.

both ignited and unignited particles near the outer edge, consistent with the predictions. However, the predicted particles heat more slowly than the measured particles near the edge of the stream and the ignited particles have a higher temperature than predicted. The higher temperature of ignited particles is probably due to not having the correct CO_2/CO ratio at the particle surface as discussed below. Also, the measured CO_2 temperature is usually higher than the predicted average gas temperature where ignition occurs, since the combustion energy is first going to heat the CO_2 which subsequently heats the other gases.

At 10.5 cm, the core is still fairly cool while many more particles have ignited at the outer edge. The predictions don't show the 20% of the high temperature particles which are observed to be ignited on the centerline. This may be due to the feedback of the energy to the particle from CO combustion not being modeled properly. For these calculations, it was assumed that the oxidation of the particle produces CO and all the energy from the CO --> CO_2 oxidation goes into the gas phase. This assumption is not in agreement with the measurements of Mitchell et al. (1988) or Tognotti et al. (1990). The assumption on the amount of CO_2 produced in the particle can be varied to test the predictions.

At 12 cm, the gas temperature leads the particle temperature by approximately 600 K, as oxygen diffuses from the surrounding air and reacts with the volatiles and CO produced by heterogeneous reaction. The latter is assumed in the model to react to CO_2 in the bulk gas, away from the particle surface. After the volatiles have reacted, the burning char particles continue to rise in temperature and exceed the temperature of the gas, even in the core. At 16 cm and higher, some particles near the outer edge have burned out and dropped in temperature to that of the gas. It is the smallest particles (45 μm) which burn out first. The predicted temperatures are higher than measured at 25 cm. This may be a problem with the reduction of reactivity at high extents of burnout.

Figure III.A-7 presents the measured height of the continuum blockage determined for soot from the transmittance spectra as percent of the incident IR beam compared with the predicted mole fraction of condensed carbon. Figure III.A-7a shows the radial profiles at 10.5 cm, the location of highest measured soot concentration, and Fig. III.A-7b shows the axial centerline profiles. As shown, the peak concentration of condensed carbon occurs at approximately 10 cm, and this coincides with the highest measured

a) Radial profile at 10.5 cm:

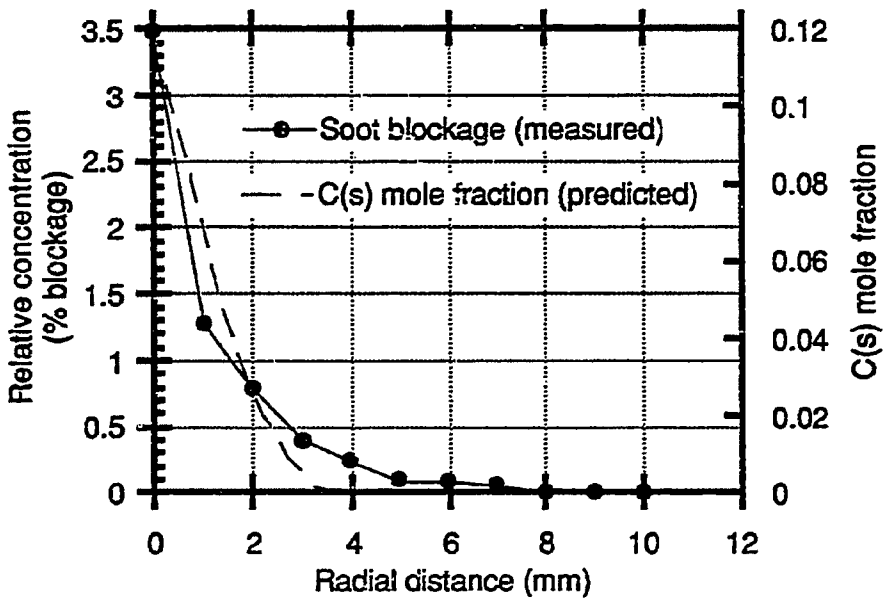

b) Axial profile at the centerline:

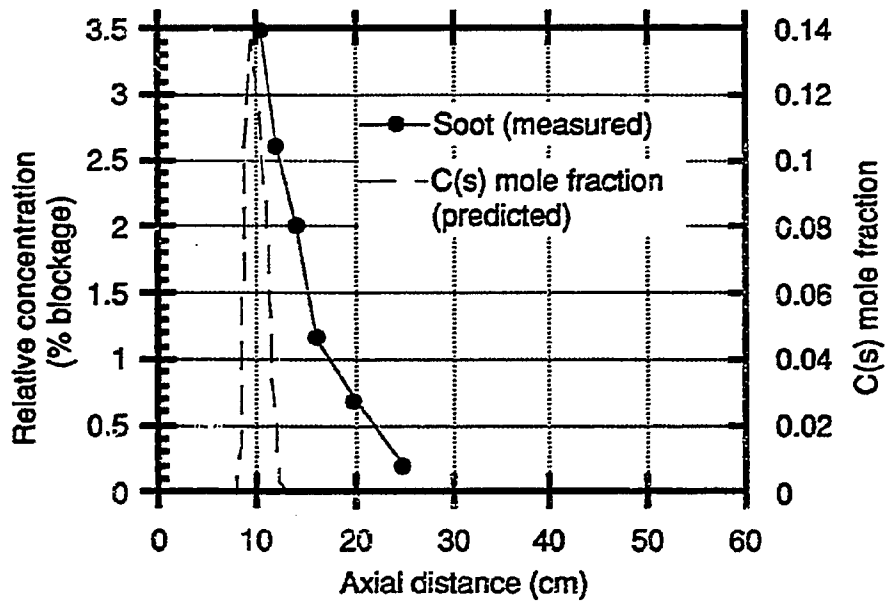

Figure III.A-7. Relative soot concentration determined by tomographic reconstruction of FT-IR emission/transmission spectra from a Rosebud coal flame in the TWR compared with predicted concentration of condensed carbon.

concentration of soot. The predicted radial profile at 10.5 cm has approximately the same shape as the measured profile. However, the decay of soot, once formed, seems to be kinetically controlled, as the predicted centerline concentration of condensed carbon falls off much more rapidly than the measured soot concentration.

Figure III.A-8 shows the measured and predicted CO_2 concentrations. The absolute values cannot be compared, because the measured values are given in absorbance units, which have not been calibrated. However, the relative magnitudes and trends show reasonable agreement. Prior to ignition, the measured and predicted concentration is low. Both measured and predicted values are higher at the centerline after ignition and remain fairly constant to a distance of 25 cm.

Conclusions - After modifying for up-firing, gas buoyancy, and laminarization, the computer model for two-dimensional, turbulent combustion of pulverized coal, PCGC-2, has been used to successfully model the laminar coal flame in the transparent wall reactor. Key flame properties, such as ignition point, burnout profile, and gas and particle temperature, have been reasonably well predicted. Complex flow patterns at the nozzle promote particle dispersion, and were not adequately resolved with current grid spacing. Code predictions are sensitive to inlet boundary conditions for the coal stream at the nozzle exit, and detailed characterization of this boundary condition is needed. Soot formation seems to correlate with equilibrium concentration of condensed carbon, but decays more slowly than predicted from equilibrium. The energy feedback to particles or the CO_2/CO ratio produced at the particle is not adequately predicted.

Graphic Interface

Work continued on the development of a graphical user interface (GUI) for PCGC-2 on the Sun workstation. A window was added for specifying the composition and temperature of the inlet streams. The thermodynamic input file can now be generated automatically using information in the main data file and a database containing data for approximately 200 species. Work was also initiated to apply two graphical programs that have been developed under independent funding, a pre- and a post-processor, to PCGC-2. The relationship of these two programs and the GUI to PCGC-2 is shown in Figure III.A-9. As shown, the pre-processor generates a computational grid and the post-processor presents code results. The format of the grid file used by PCGC-2 differs

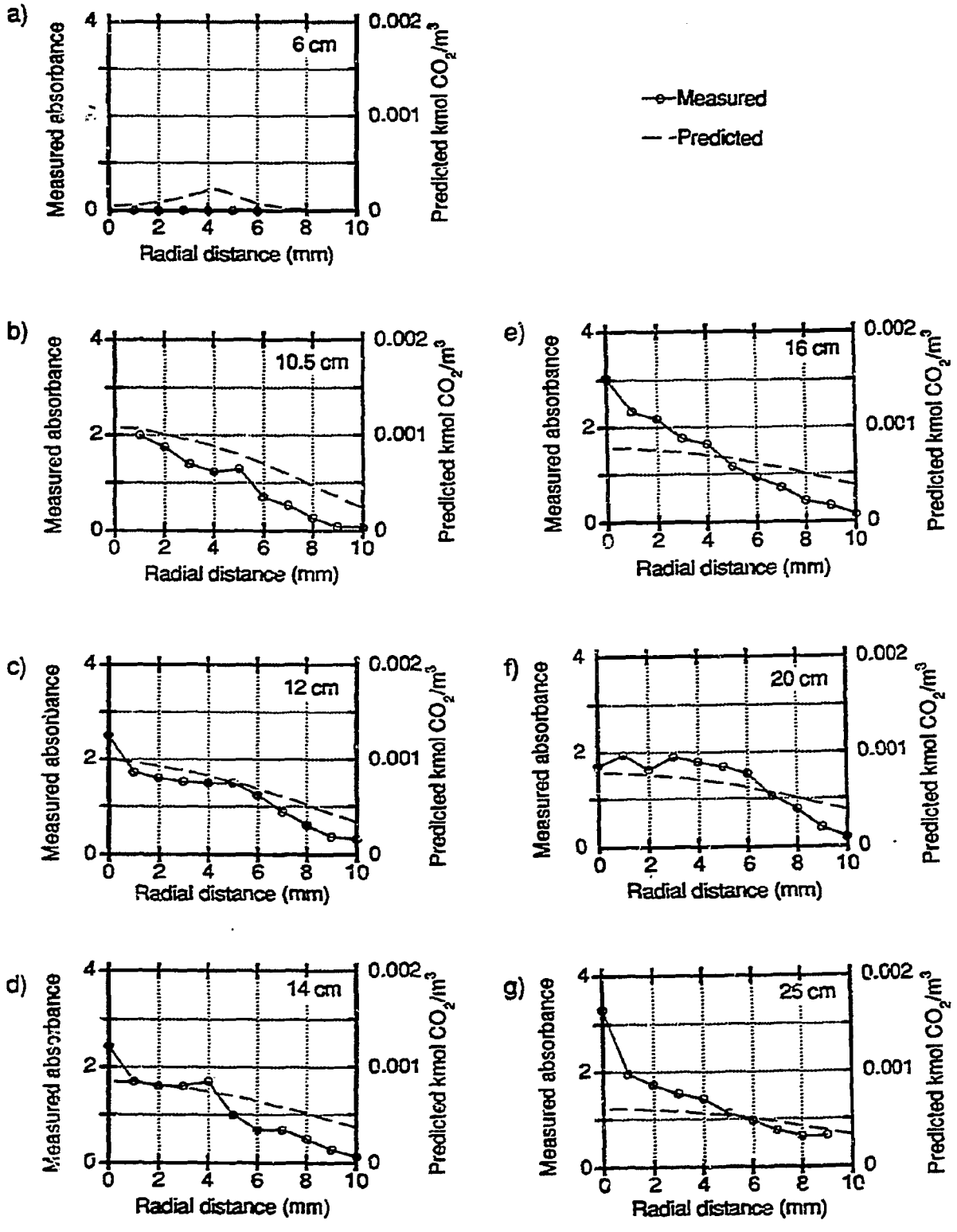

Figure III.A-8. Radial CO_2 absorbance profiles determined from tomographic reconstruction of FT-IR emission/transmission spectra compared with predicted CO_2 concentration for a Rosebud subbituminous coal flame in the TWR.

from that used by the pre-processor, and a program was written for converting files between the two formats. A subroutine was modified and added to PCGC-2 for writing the plotting file needed by the post-processor.

Both the pre- and post-processors have been applied to the TWR simulation described above. Figure III.A-10a shows the graphical representation of the computational grid, and Figure III.A-10b shows the computed gas temperature. The vertical lines in the grid are the radial node locations and the horizontal lines are the axial nodes. The reactor centerline is to the left, where the radial nodes are more closely spaced. The light blue strip on the right side of the grid represents the reactor wall. The cells representing the coal feed tube are at the lower, left-hand corner. They are color-coded, but can't be seen in this figure. The cells representing the preheated air inlet are the cells colored red at the bottom. The cells colored green represent the room air inlet. The buttons along the top and right-hand side of the window allow the user to select different code options to construct and modify the grid.

The color-fringe plot in Figure III.A-10b is on its side, with the reactor inlet on the left and the gas flowing to the right. The centerline is at the bottom and the wall is at the top. The yellow and red regions indicate the location of the flame and hot combustion gases. The coal inlet stream can be seen at the lower, left-hand corner. The postprocessor also has buttons across the top (not visible in this figure) and down the right-hand side of the window to allow the user to interact with the program.

Plans

Early in the next quarter, work will be completed on modeling of the TWR reactor flames. Work will continue on extending the graphical user interface. A major effort will be initiated toward development of the final integration of PCGC-2 and FG-DVC, including user-friendliness, robustness, and the user's manual. The first version of the graphical interface will be completed for gas, and consideration will be given to extending to particles. A poster paper entitled "Structure of a Near-Laminar Coal Jet Diffusion Flame" will be presented at the 23rd Symposium (International) on Combustion to be held in Orléans, France, on July 22-27.

a) Computational grid (pre-processor)

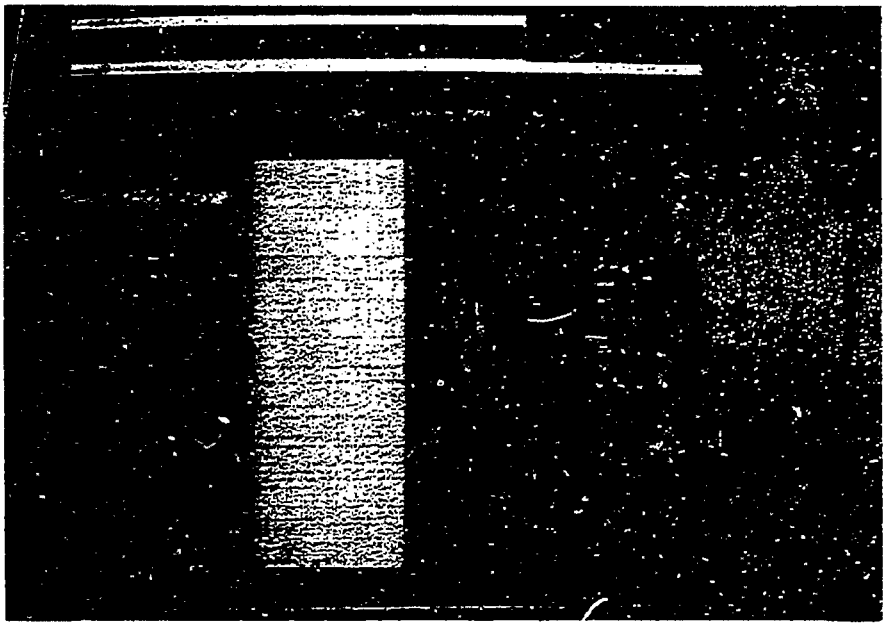

b) Predicted temperature field (post-processor)

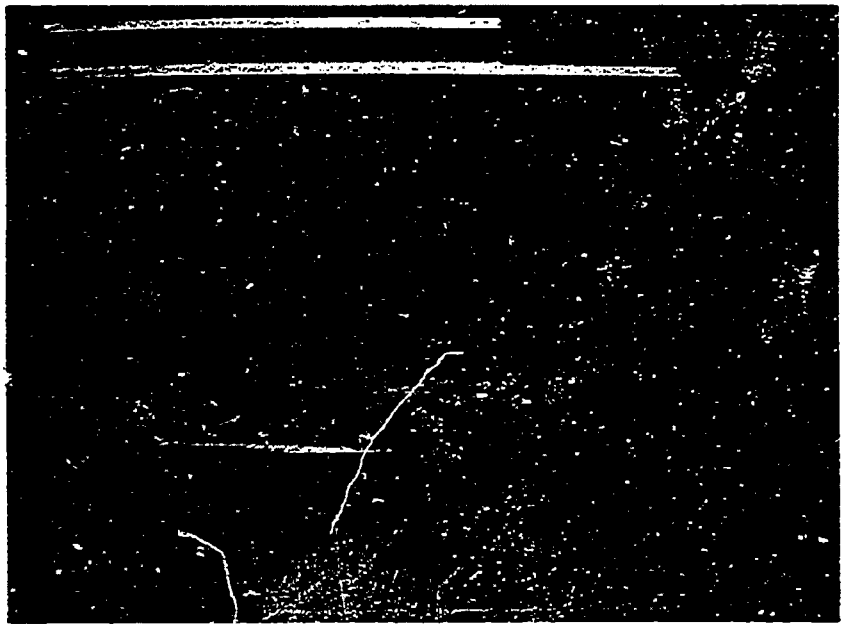

Figure III.A-10. Computational grid and predicted temperature field as rendered by the pre- and post-processors on a Sun workstation for the PCGC-2 simulation of the Montana Rosebud subbituminous coal flame in the transparent wall reactor.

III.B. SUBTASK 3.B. - COMPREHENSIVE FIXED-BED MODELING REVIEW, DEVELOPMENT, EVALUATION, AND IMPLEMENTATION

Senior Investigators - Predrag T. Radulovic and L. Douglas Smoot
Brigham Young University
Provo, Utah 84602
(801) 378-3097 and (801)378-4326

Graduate Research Assistant - Michael L. Hobbs

Objectives

The objectives of this subtask are 1) to develop an advanced fixed-bed model incorporating the advanced submodels being developed under Task 2, particularly the large-particle submodel (Subtask 2.e.), and 2) to evaluate the advanced model.

Accomplishments

During the last quarter, work continued on reviewing, coding, and validating submodels. To enhance user-friendliness, the input file has been rewritten to segregate input parameters for the two-zone submodel and the one-dimensional submodel. Also, the fixed-bed code has been rewritten in a modular fashion with extensive comment statements. The two-zone submodel has been improved to accommodate user-specified burnout. Also, two heat transfer zones were added to the well-mixed model to account for heat loss in the freeboard region and heat transfer between solid and gas in the ash zone of the reactor. The ash enthalpy calculation was improved. The heat capacity of the ash is calculated with the Kopp-Neumann rule which is based on the various constituents of the ash. Melting is assumed to occur at the measured ash fluid temperature, and the associated enthalpy of fusion is assumed to be 230 J/g (Mills and Rhine, 1989).

The fixed-bed code was evaluated by parametric sensitivity analysis. Sensitivity runs were divided into model options, model parameters and operational parameters. Model options include tar vapor reaction equilibrium, volatile mass transport, char ash layer formation, and combustion product distribution. Model parameters include the solid-to-gas heat transfer coefficient, effective diffusivity, bed-to-wall heat transfer, potential tar-forming fraction, functional group composition (coal rank), and oxidation and

gasification kinetics. Operational parameters include the temperature of the feed gas, reactor pressure, coal mass flow rate, steam mass flow rate, air mass flow rate, while coal and bed properties include proximate ash content of the feed coal, proximate moisture content of the feed coal, particle diameter, and bed void fraction.

Calculations have been conducted for twelve coal types which range from lignite to bituminous. The availability of experimental profiles within laboratory-scale or commercial-scale fixed-bed gasifiers is limited. Temperature and pressure profiles have been measured by Thimsen et al. (1984) during coal gasification in a Wellman-Galusha gasifier. True density, particle density, bulk (bed) density, bed void fraction, porosity, particle diameter, and carbon conversion for feed coal and exit ash were determined from available experimental data and correlations provided in Elliott (1981).

Improved Two-Zone Submodel

The two-zone submodel was refined by adding two heat transfer zones to account for heat loss in the freeboard region and heat transfer between solid and gas in the ash zone of the reactor. In the ash zone, the solid and gas temperatures are close and, therefore, a reasonable assumption is to assume them equal. However, this assumption has little effect on calculated effluent results since the ash mass flow rates are typically small in fixed-bed reactors.

Improved Ash Enthalpy

The specific heat of the ash, $Cp_a\ (\frac{J}{kg \cdot K})$, can be determined from (Merrick, 1983):

$$Cp_a = 754 + 0.586t \qquad \text{(III.B-1)}$$

where $t(^{\circ}C)$ is the ash temperature. The Kopp-Neumann rule also gives reliable estimates of the ash heat capacity if the various constituents of the ash are known (Mills and Rhine, 1989):

$$Cp_a = \frac{1000 * \sum_{i=1}^{n} x_i Cp_i}{\bar{M}_w} \qquad \text{(III.B-2)}$$

where x_i, $Cp_i\left(\frac{J}{mol \cdot K}\right)$, and $\bar{M}_w$ represent the mole fraction of the i^{th} ash constituent, partial molar heat capacity of the pure i^{th} component, and the weight-average molecular weight of the ash or slag. The temperature

dependence of C_p is frequently expressed as $C_p = a + bT - cT^{-2}$ and values of a, b, and c for slag constituents used herein are given in Table III.B-1. Equation III.B-2 can also be used to determine the heat capacity of the liquid slag. Melting is assumed to occur at the measured ash fluid temperature, and the associated enthalpy of fusion is assumed to be 230 $\frac{J}{g}$ (Mills and Rhine, 1989).

Sensitivity Analysis

The one-dimensional model sensitivity analysis is divided into three major sections: 1) model options, 2) model parameters, and 3) operational and coal parameters. Details regarding each option and input parameters are available in Hobbs (1990). The base case is gasification of Jetson bituminous coal in an atmospheric, air-fired, Wellman-Galusha gasifier. Four model options are briefly discussed herein. The model options include tar vapor reaction equilibrium, volatiles mass transport, char ash layer formation, and combustion product distribution. Three model parameters are also discussed: solid-to-gas heat transfer, effective diffusivity, and bed-to-wall heat transfer. Six operational and coal parameters are discussed: potential tar-forming fraction (relates to coal rank), feed gas temperature, reactor pressure, feed coal flow rate, particle size, and bed void fraction.

The sensitivity analysis reported in this section is taken from approximately 300 simulations. Only 38 of these simulations are given in Figures III.B-1 and III.B-2. The extra simulations were performed to determine the most appropriate set of realistic fixed-bed parameters. Additional information and details regarding the fixed-bed sensitivity can be found in Hobbs (1990).

Tar Vapor Reaction Equilibrium - The one-dimensional, fixed-bed model has two options for treating tar vapor chemistry: 1) the tar is allowed to react in the gas phase to completion (chemical equilibrium assumption) or 2) the tar vapor is nonreactive (i.e., in thermal equilibrium, but "frozen" chemically). "Condensed-phase" tar is included in the char. If Option 1 is chosen, all gases including tar are assumed to be in chemical equilibrium. If Option 2 is chosen, all gases except tar are assumed to be in chemical equilibrium.

The predicted sensitivity of the axial solid temperature profile to the tar gas phase equilibrium assumption is shown in Figure III.B-1a. Use of the equilibrium assumption causes the temperature peak to shift closer to the

Table III.B-1. Partial molar heat capacity of slag components used in Kopp-Neumann rule.[§]

Slag	M_w	$\bar{C}p_i\left(\frac{J}{molK}\right) = a + bT - CT^{-2}$			$\bar{C}p$ (liquid)
Component	$\frac{kg}{kmol}$	a	b	c	$\frac{J}{molK}$
SiO_2	60.09	53.591	1.8715×10^{-2}	1.2644×10^{6}	87.0
CaO	56.08	41.868	2.0264×10^{-2}	4.5217×10^{5}	80.8
Al_2O_3	101.96	92.445	3.7560×10^{-2}	2.1876×10^{6}	146.4
MgO	40.31	45.469	5.0116×10^{-3}	8.7379×10^{5}	90.4
K_2O‡	94.2	65.700	2.2600×10^{-2}	0.0	74.0
Na_2O‡	61.98	65.700	2.2600×10^{-2}	0.0	92.0
TiO_2	79.9	49.446	3.1368×10^{-2}	1.7543×10^{5}	111.7
MnO	70.94	31.108	4.3459×10^{-2}	5.5156×10^{-5}	79.9
FeO	71.85	52.84	6.2470×10^{-3}	3.1903×10^{5}	76.6
Fe_2O_3	159.7	103.50	6.7156×10^{-2}	1.7727×10^{6}	191.2
Fe‡	55.85	12.72	3.1710×10^{-2}	-2.5100×10^{5}	43.9
P_2O_5‡	141.91	182.5	4.6400×10^{-2}	4.5440×10^{6}	242.7
CaF_2‡	78.08	59.83	3.045×10^{-2}	-1.9600×10^{5}	96.2
SO_3‡	80.06	70.2	9.774×10^{-2}	0.0	175.7

§ All solid heat capacity coefficients obtained from Perry's Handbook (1973 page 3-119) except as noted. All liquid heat capacity values are obtained from Mills and Rhine (1989).

‡ Solid heat capacity coefficients obtained from Mills and Rhine correcting b and c by 10^{-3} and 10^{5}, respectively.

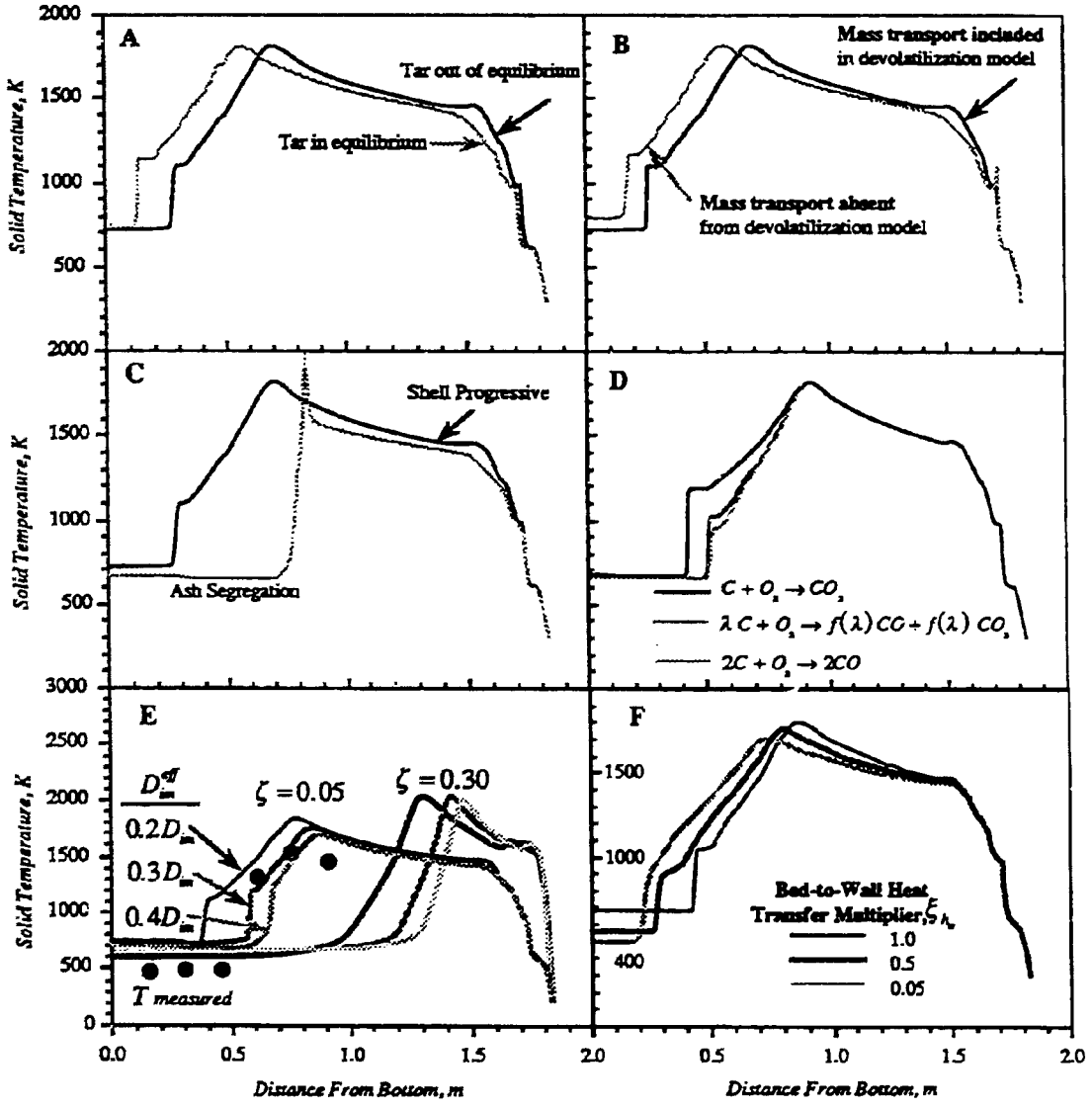

Figure III.B-1 Predicted sensitivity of axial solid temperature to A) tar gas phase equilibrium assumption, B) the devolatilization mass transport option, C) char model ash assumption, D) combustion product distribution assumption E) solid-to-gas heat transfer correction factor, ζ, and effective diffusivity and F) bed-to-wall heat transfer multiplier. These results are for the Wellman-Galusha gasifier and Jetson bituminous coal. Complete input conditions can be found in Hobbs (1990).

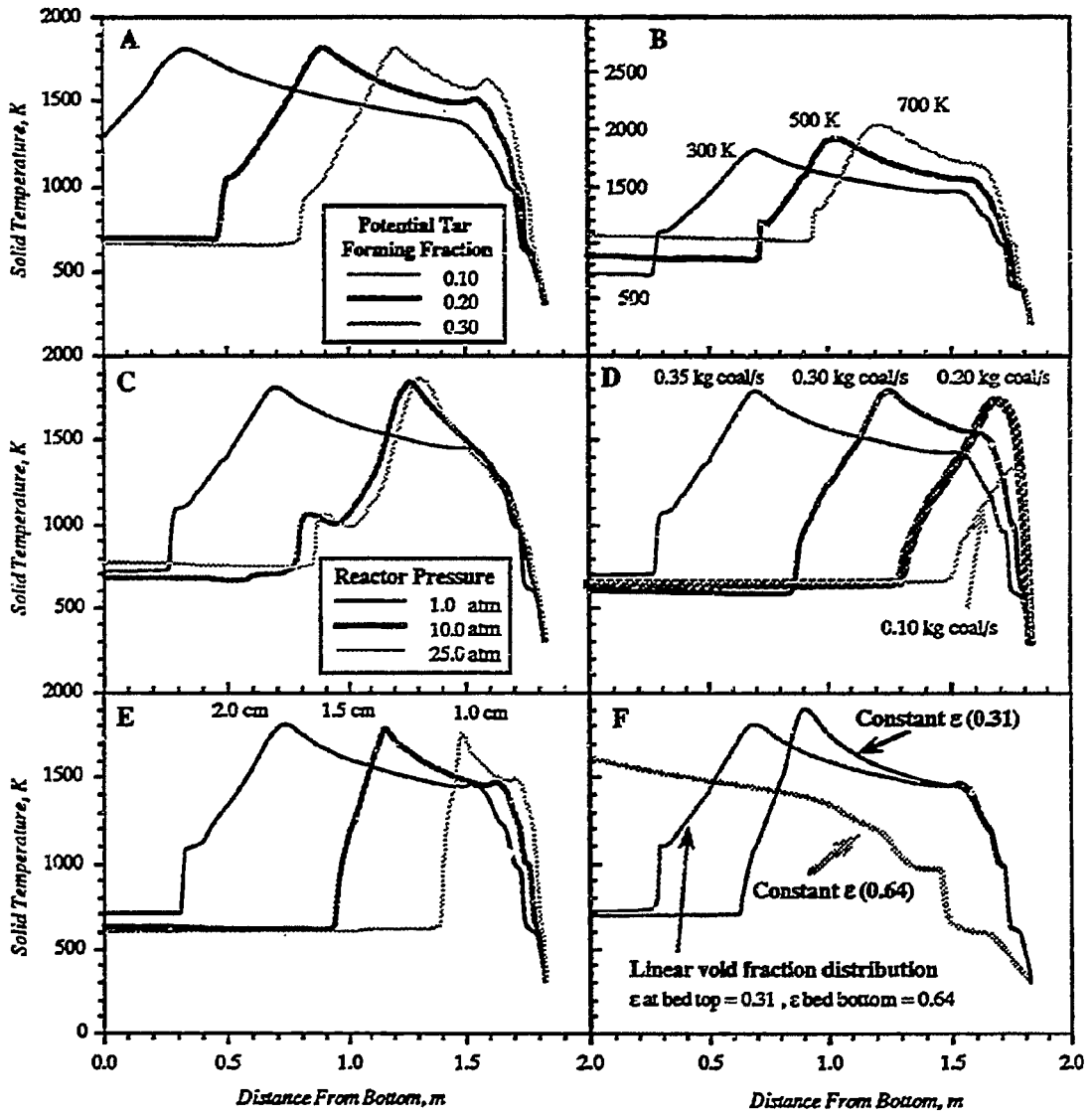

Figure IILB-2 Predicted sensitivity of axial solid temperature to A) potential tar forming fraction, B) feed gas temperature, C) pressure, D) feed coal mass flow rate, E) particle diameter, and F) Bed void fraction. These results are for the Wellman-Galusha gasifier and Jetson bituminous coal. Complete input conditions can be found in Hobbs (1990).

bottom of the reactor. This shift can be explained by noting that the gasifier is fuel-rich near the top. When the tar is allowed to react to equilibrium in the drying and devolatilization zones, the gas phase becomes more fuel-rich, which causes the temperature to decrease slightly. This decrease in temperature leads to an increased devolatilization zone length which consequently causes the entire temperature profile to shift downward. The transition between the devolatilization and gasification zones is more gradual when the tar is allowed to react to equilibrium. Again, the gradual transition is attributed to lower temperatures.

Volatiles Mass Transport - Two options regarding volatiles mass transport were investigated: 1) mass transport is included via transport resistances through the film and particle similar to char oxidation and gasification or 2) mass transport is not included. The predicted sensitivity of axial solid temperature to the volatile mass transport is shown in Figure III.B-1b. When mass transport is not considered during devolatilization, a temperature spike occurs in the devolatilization zone which is attributed to the rapid release of volatile matter into the gas phase. The temperature shift in the overall solid temperature curve can be explained in a manner which is similar to the sensitivity analysis of the tar vapor reaction equilibrium assumption. The rapid release of volatile matter near the reactor top causes the gas phase to become more fuel-rich which causes the temperature to decrease. The decreased temperature in the devolatilization zone causes the zone length to increase which causes the location of the maximum temperature to move toward the bottom of the reactor.

Char Ash Layer Formation - The ash in the shell progressive (SP) char oxidation submodel is assumed to remain intact, surrounding the unreacted char core. The oxidant is required to diffuse through the gas film and ash layers. The ash in the ash segregation (AS) model is assumed to be removed instantaneously and fall away from the char particle with the oxidant required only to diffuse through the film boundary layer. The predicted sensitivity of axial solid temperature to the SP and AS ash assumptions is shown in Figure III.B-1c. The shape of the solid temperature profile using the AS model is sharp compared to the broad peak predicted by using the SP model. Also, the maximum temperature is higher when the AS model option is chosen. Furthermore, the devolatilization zone temperature is lower for the AS model option.

Increasing the equivalence ratio in a fuel-rich zone, such as in the drying, devolatilization, or gasification zones, causes the temperature to decrease. Conversely, in a fuel-lean zone, such as the oxidation zone, increasing the equivalence ratio will cause the temperature to increase. Both an increase and decrease in temperature in fuel-lean and fuel-rich regions in the gasifier can be observed in Figure III.B-1c. The AS submodel option results in an increased rate of carbon being added to the gas phase, which causes the gas phase to become more fuel-rich. In the drying, devolatilization, and gasification zones, a decrease in temperature is observed. Typically, lower devolatilization temperatures cause the location of the maximum temperature to shift downward. However, the location of the maximum temperature in Figure III.B-1c shifts toward the top of the reactor. The shift upward is attributed to a significantly shorter oxidation zone caused by increased carbon release into the fuel-lean gas phase. The two models should represent extremes in possible ash behavior, although the SP model is expected to be closer to actual ash behavior. This conclusion is based on comparing predicted temperature profiles to measured profiles, and is discussed in more detail in the validation sections of this chapter.

Combustion Product Distribution - The oxidation of carbon produces both CO and CO_2 as primary products. Carbon monoxide may be favored at higher temperatures if CO is formed at carbon edges and CO_2 is formed at inorganic sites. Lower temperatures may favor CO_2 due to catalytic activity (Laurendeau, 1978).

Predicted sensitivity of axial solid temperature to the distribution of CO and CO_2 is shown in Figure III.B-1d. Three assumptions are shown: 1) CO_2 as the sole primary combustion product, 2) CO as the sole primary combustion product, and 3) a distribution of CO_2 and CO combustion products that depends on solid temperature. As expected, only the oxidation zone is affected by the combustion product distribution assumption. The different temperatures are attributed to the energy exchange at the particle-to-gas interface due to reaction. Comparison between the sole CO distribution and the CO/CO_2 distribution indicates that carbon monoxide may be assumed to be the primary product at typical combustion temperatures. Laurendeau (1978) makes this same conclusion.

Solid-to-Gas Heat Transfer Coefficient - The solid-to-gas heat transfer coefficient for a nonreacting system may be ten to fifty times higher than for

a reacting system (Lowry, 1963). Dzhaphyev et al. (1986) attribute the difference in computed values to unsteady heat transfer. Vigorous reactions as well as nonsphericity may also contribute to this discrepancy. The solid temperature is sensitive to the ratio of reactive to non-reactive heat transfer coefficients, ζ , which ranges between 1.0 and 0.02. Predicted sensitivity of axial solid temperature to solid-to-gas heat transfer correction factor, ζ, is shown in Figure III.B-1e.

This solid-to-gas heat transfer correction factor (ζ) has a dramatic effect on the location of the maximum solid temperature. Small values of ζ cause the location of the maximum temperature to shift toward the bottom of the reactor. By limiting the heat exchange between solid and gas at the top of the reactor, the solid temperature decreases in the devolatilization zone, which increases the length of the devolatilization zone. The increased size of the devolatilization zone causes the entire temperature profile to shift toward the bottom of the reactor. Also, the magnitude of the maximum temperature decreases as ζ is decreased. The decrease in maximum temperature is attributed to a redistribution of solid enthalpy.

Effective Diffusivity - The oxidation and gasification rates are globally modeled by using an effective diffusivity which is based on the molecular diffusivity multiplied by a constant ($D_{eff} = \phi D_m$). The constant, ϕ , is based on the porosity of the developing ash layer. Thorsness and Kang (1985) used 0.35 for ϕ. Laurendeau (1978) showed that ϕ can be estimated by the ash porosity divided by two. The value two is an estimate of the tortuosity squared. Wang and Wen (1972) have measured porosity of a fire clay ash which varied from 0.4 to 0.8. Using Wang and Wen's values for the ash porosity (0.4 to 0.8), ϕ should range between 0.2 and 0.4.

Although the ash porosity for the sensitivity analysis is assumed to range between 0.4 and 0.8, the ash porosity should not be limited to these values. The ash porosity can be determined by using extrapolated values of pore volume (Elliott, 1981, page 1520, Figure 23.14). The ash porosities for the for high-pressure, fixed-bed gasification may range between 0.1 and 0.3 (with corresponding ϕ ranging between 0.05 and 0.15) which implies significant compaction for the fixed-bed ash compared to the measurements of Wang and Wen (1972).

The predicted sensitivity of the axial solid temperature profile to the effective diffusivity is shown in Figure III.B-1e. The effective diffusivity

affects the location of the maximum solid temperature, the magnitude of the maximum solid temperature and the shape of the solid temperature profile. Lower values of ϕ cause the location of the maximum solid temperature to shift toward the bottom of the reactor and the size of the oxidation zone to increase. The impact of the effective diffusivity on solid temperature may be a consequence of the size and shape of the reactant. For example, the molecular diffusivity for oxygen is smaller than the molecular diffusivity for steam. In other words, the oxygen diffusive resistance is greater than the steam diffusive resistance. Thus, smaller values of ϕ influence the steam gasification reaction less than the oxidation reaction. Therefore, the endothermic oxidation reaction is favored for lower values of ϕ which may explain the higher maximum solid temperature.

Bed-to-Wall Heat Transfer - The sensitivity of solid axial temperature to the bed-to-wall heat transfer calculation is shown in Figure III.B-1f. For the calculations, the effective bed-to-wall heat transfer coefficient was multiplied by a constant, ζ_{hw}, to see the effect of lowering bed-to-wall heat transfer. Lower values of ζ_{hw} caused the overall axial solid temperature to decrease in the gasification and oxidation regions of the gasifier. The opposite effect is shown in the oxidation zone where solid temperature increases. The shift in location of the maximum solid temperature and the change in the shape of the curve is attributed to a redistribution of solid enthalpy.

Potential Tar-Forming Fraction - The potential tar forming fraction, x^o, represents the maximum possible tar yield of a given coal. However, the maximum tar yield is never achieved due to competition from light gas evolution. Predicted sensitivity of axial solid temperature to the potential tar-forming fraction is shown in Figure III.B-2a. As the potential tar fraction is increased, the ultimate volatile yield increases and the corresponding ultimate char yield decreases, which results in a larger devolatilization zone and a smaller gasification/oxidation zone. The shift in the location of the maximum solid temperature can be attributed to the smaller oxidation and gasification zones.

Temperature of Feed Gas - The predicted sensitivity of axial solid temperature and axial gas composition to feed gas temperature is shown in Figure III.B-2b. The location of the maximum temperature and the magnitude of the maximum temperature are affected by feed gas temperature. As expected, the maximum temperature is lower when the feed gas temperatures are lower.

The location of the maximum temperature at steady operating conditions shifts toward the bottom of the reactor when the feed gas temperature is lowered. The lower feed gas temperature causes the effluent gas temperature to decrease. The lower effluent gas temperature results in less sensible energy to preheat and dry the feed coal. Thus, both the drying and devolatilization zone lengths are increased, which causes the location of the maximum temperature to move toward the bottom of the reactor as shown in Figure III.B-2b.

Reactor Pressure - The predicted sensitivity of axial solid temperature and gas concentrations to reactor pressure is shown in Figure III.B-2c. The nonlinear effect of pressure results in the formation of a duel peak in the oxidation zone. The "duel" peak also was observed during the validation simulations of the high pressure dry-ash Lurgi gasifiers (Hobbs, 1990). Increasing pressure causes the location of the maximum temperature to shift toward the top of the reactor. The shift caused by pressure is very nonlinear. In fact, simulations at 50 and 100 atmospheres were close to the 25-atmosphere simulation plotted in Figure III.B-2c. The small peak near the bottom of the reactor is attributed to competition between the highly exothermic oxidation reaction and the endothermic steam gasification reaction.

Once the solid temperature is sufficiently high for the oxidation reaction to begin, the oxidation reaction is very rapid. The rapid oxidation of carbon causes the solid temperature to increase dramatically. Once the temperature reaches about 1000 K, the steam reaction begins. Although the steam reaction is not as fast as the oxidation reaction, the concentration of steam is significantly higher than the oxygen concentration. The carbon consumption associated with the steam reaction approaches carbon consumption associated with the oxidation reaction. The endothermic steam gasification reaction quenches the rapid increase in solid temperature and causes a sudden increase in the solid temperature profile which is observed in the low-pressure case in Figure III.B-2c.

When pressure is increased, the partial pressure of the water increases. Although the partial pressure of oxygen is also increased, the greater abundance of steam causes an increase in the steam gasification reaction when compared to the oxidation reaction. The effect is to magnify the competition between the endothermic and exothermic reactions, producing a small peak. Also, the diffusivity of water is greater than that of oxygen. In other words, the oxygen mass diffusive resistance is greater than the steam diffusive resistance. Changes in pressure have a greater effect on the

oxidation reaction than on the steam gasification reaction. Therefore, the steam gasification reaction is amplified at higher pressures.

Coal Mass Flow Rate - The predicted sensitivity of axial solid temperature to coal mass flow rate is shown in Figure III.B-2d. All parameters in these simulations were held constant except the coal mass flow rate. The shift in the location of the maximum temperature is attributed to a decrease in time required to completely consume all of the organic matter in the coal. It is interesting to note that the low coal mass flow rates actually correspond to combustion occurring at the top of the gasifier. Thus, both combustion and gasification runs are also depicted in Figure III.B-2d.

Particle Diameter - The predicted sensitivity of axial solid temperature to feed coal particle diameter is shown in Figure III.B-2e. The small particles heat up faster than the larger particles. The increased solid temperature promotes devolatilization, which is completed more quickly than for the larger particles. Also, mass transport limitations are not as pronounced for the smaller particles.

The particle size effect seems to be approximately linear as shown in the temperature profile in Figure III.B-2e. However, the influence of a distribution of particles may be difficult to determine. Not only are heat and mass transport processes affected significantly, but also the bed void fraction may change dramatically as discussed in the following section. Wide particle size distributions tend to decrease the bed void fraction.

Bed Void Fraction - The predicted sensitivity of axial solid temperature to bed void fraction is shown in Figure III.B-2f. The void fraction significantly affects the particle number density which in turn affects the overall bed consumption rate. Increasing void fraction causes a decrease in the overall bed reaction rate. Drying, devolatilization, gasification and oxidation rates are decreased significantly when the void fraction is increased. Thus, all prominent reaction zones increase with increasing bed void fraction and the location of the maximum temperature moves toward the bottom of the reactor.

The abrupt changes taking place in the solid temperature profile are magnified in the case where the void fraction is assumed to be constant at 0.54 in Figure III.B-2f. The initial increase in temperature is attributed to evolution of loose functional groups. The sudden increase in solid

temperature at the reactor top is attributed to a rapid release of tar. Finally, the tight functional groups evolve slowly until devolatilization is complete.

Model Evaluation

This section treats evaluation of the one-dimensional, fixed-bed model by comparing predictions with experimental data and modeling results of other investigators. Unfortunately, the availability of experimental profiles within laboratory scale or commercial scale fixed-bed gasifiers is limited. Temperature and pressure profiles have been measured by Thimsen et al. (1984) during coal gasification in a Wellman-Galusha gasifier.

Thimsen (1990) suggests that the Wellman-Galusha measured temperature profiles be used only for qualitative comparisons since the temperature probe, a 1/2-inch Schedule 40 304 SS pipe with six sheathed type K thermocouples placed six inches apart, was retracted from the gasifier when any junction approached 1600 K. The rod was retracted for protection from high temperature. Typically, the temperature probe was allowed ten minutes to reach a steady state (Thimsen et al., 1984). However, the temperature profiles may represent transient conditions if the probes were retracted due to high temperatures.

Lurgi Simulation - Predicted temperature, pressure drop, gas concentration, carbon consumption, burnout, and particle diameter for gasification of Illinois #6 coal in a high-pressure, oxygen-fired Lurgi gasifier are shown in Figure III.B-3. Input conditions, including true, particle and bulk densities, bed void fraction, porosity, particle diameter and carbon conversion for feed coal and exit ash can be found in Hobbs (1990).

The high-pressure, oxygen-fired Lurgi cases produce a sigmoid or S-shaped CO_2 concentration profile. The shape of the carbon dioxide profile can be explained by the low temperature of the solid in the gasification section of the gasifier. The low temperature is a result of large quantities of steam in the feed gas stream. The temperature is low enough that the only significant heterogeneous reaction in this section of the gasifier is the steam gasification reaction. Gasification with carbon dioxide is essentially quenched due to low temperatures. With only hydrogen and carbon monoxide being produced in the gasification section, the hydrogen and carbon monoxide profiles should correspond. However, gas phase reactions such as the water-

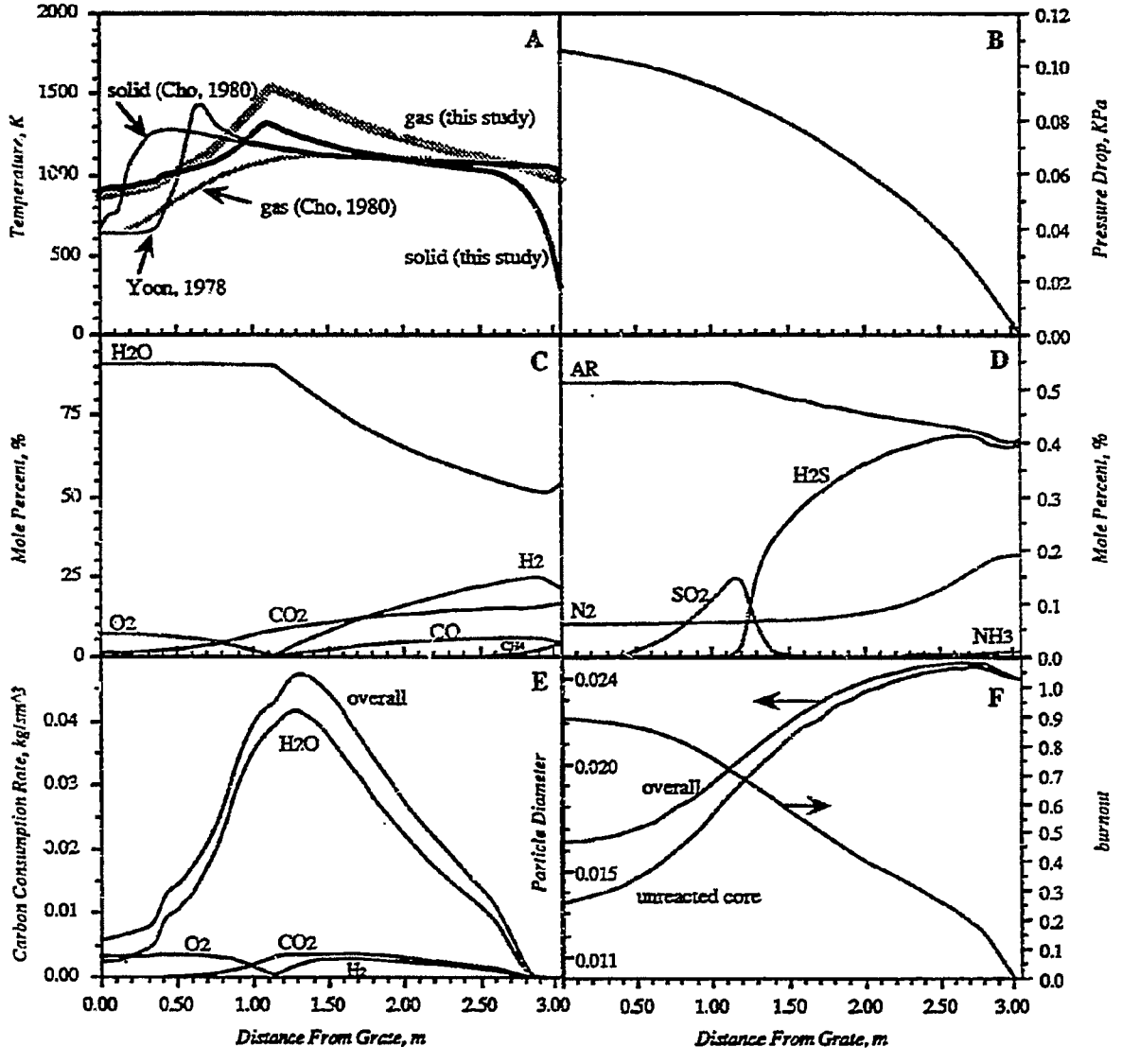

Figure III.B-3 Predicted temperature, pressure drop, gas concentration, carbon consumption due to oxidation and gasification, burnout, and particle diameter for gasification of Illinois #6 bituminous coal in high pressure gasifier with oxygen (Elgin and Perks, 1974): A) solid and gas temperature profile, B) pressure drop, C) major species concentration profile, D) minor gas species concentration profile, E) volumetric solid carbon consumption rate due to oxidation and gasification reactions, and F) burnout, overall and unreacted particle diameter throughout reactor. Input conditions can be found in Hobbs (1990). Part A shows results from the homogeneous model of Yoon (1979) and the heterogeneous model of Cho (1980). Yoon and Cho report that the input conditions for the cases shown in Part A are for gasification of Illinois #6 in the high pressure Lurgi gasifier at Westfield. However, the input conditions are slightly different from that reported by Elgin and Perks (1974).

gas-shift reaction produce a slight increase in carbon dioxide concentration, creating a sigmoid profile.

Predictions from two one-dimensional models from the literature are also shown in Figure III.B-3a. Yoon assumed equal solid and gas temperature, instantaneous devolatilization with a fixed composition, and assumed that the water-gas-shift reaction determines the gas phase concentration. Cho essentially extended the model of Yoon to include separate solid and gas temperatures. The sharp spike predicted by Yoon probably results from noncompeting endothermic and exothermic reactions. Also, the average solid and gas temperatures of Cho do not correspond to the predictions of Yoon. Cho's gas temperatures are less than the solid temperature in the oxidation zone. Steam gasification produces H_2 and CO in the oxidation zone. Also, CO is produced from oxidation. In the presence of oxygen, the homogeneous reactions of H_2 and CO with O_2 react to produce H_2O, CO_2 and heat. These exothermic gas phase reactions inevitably cause a dramatic increase in gas temperature, as shown in the predictions presented in this study.

Since there are no measurements of axial temperature or concentration profiles in the Lurgi gasifiers, it is difficult to conclude which simulations are correct. All models seem to predict reasonable effluent properties even though the profiles are significantly different.

Wellman-Galusha Simulation - Predicted temperature, pressure drop, gas concentration, carbon consumption, burnout, and particle diameter for gasification of Utah Blind Canyon bituminous coal in an atmospheric, air-fired Wellman-Galusha gasifier are shown in Figure III.B-4. Input conditions including true particle and bulk densities, bed void fraction, porosity, particle diameter and carbon conversion for feed coal and exit ash can be found in Hobbs (1990).

Qualitative agreement was obtained for both the temperature profile and the pressure profile. The low measured pressure drop near the top of the reactor appears to be due to channeling near the bed top. The measured temperature profile indicates a drying and devolatilization zone length of approximately 0.5 meters which corresponds directly with the predicted drying and devolatilization zone length of 0.5 meters.

The Wellman-Galusha gas phase concentration profile can be explained by following the solid temperature profile, starting at the bottom of the

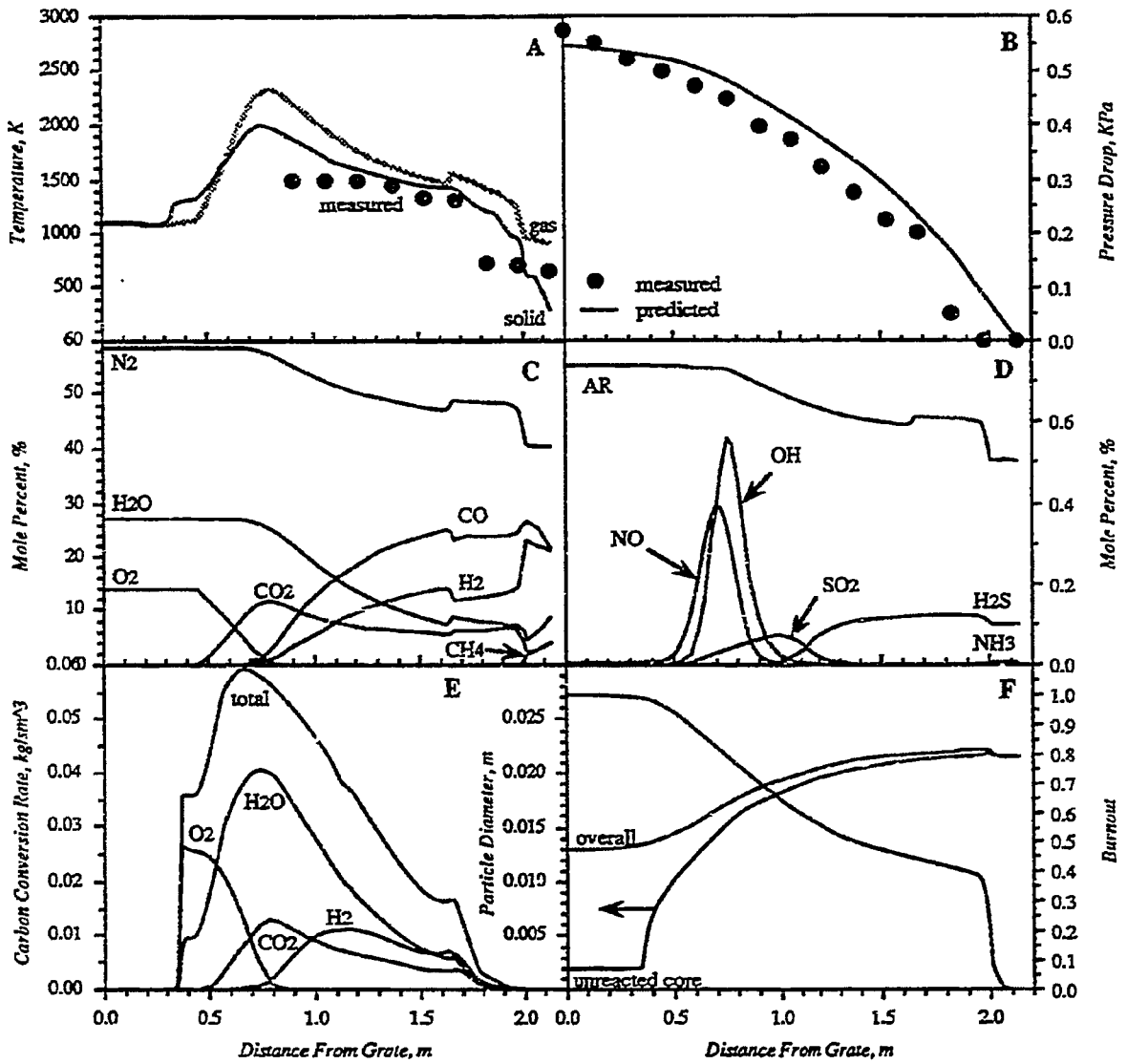

Figure III.B-4 Predicted temperature, pressure drop, gas concentration, carbon consumption due to oxidation and gasification, burnout, and particle diameter for gasification of Utah Blind Canyon bituminous coal in an atmospheric gasifier with air (Thimson et al., 1985; Vol 13, page L3): A) measured and predicted temperature profile, B) measured and predicted pressure drop, C) predicted major species concentration profile, D) predicted minor gas species concentration profile, E) predicted volumetric solid carbon consumption rate due to oxidation and gasification reactions F) predicted burnout, overall and unreacted particle diameter throughout reactor. Input conditions can be found in Hobbs (1990).

reactor. At the reactor bottom, primarily ash is present which exchanges energy with the countercurrent gas stream. As the solid increases in temperature, oxygen in the feed gas reacts heterogeneously with the solid carbon to form gaseous carbon monoxide and carbon dioxide. The carbon monoxide reacts homogeneously in the gas phase to form carbon dioxide. Steam also reacts with the solid carbon to form hydrogen and carbon monoxide. If oxygen is present in the gas phase, the hydrogen and carbon monoxide react homogeneously with oxygen to form steam and carbon dioxide. Thus, no depletion of steam is apparent until all gas phase oxygen is depleted. Furthermore, only carbon dioxide is shown to increase in the presence of homogeneous oxygen. Although both steam and carbon dioxide react heterogeneously with the solid carbon, the gasification products from both reactions are oxidized to form carbon dioxide in the presence of oxygen.

Comparison of Temperature Profiles at Different Conditions - Several of the Wellman-Galusha experimental test cases included temperature profiles at different operating conditions. Predicted temperature profiles are compared to measurements for the Elkhorn bituminous case, the Jetson bituminous case, the Leucite Hills subbituminous case and the Utah Blind Canyon bituminous case in Figs. III.B-5 and 6. Input conditions can be found in Hobbs (1990) or Thimsen et al. (1984).

The Elkhorn case shows a shift in the measured temperature profile near the top of the reactor as shown in Figure III.B-5a. The predictions are in agreement with the direction of the temperature shift. The Jetson case depicted in Figure III.B-5b shows the effect of varying operational parameters in the oxidation zone, which gives a definite indication of the change in location of the maximum temperature. Again, the direction of shift is predicted by the one-dimensional model.

The one-dimensional model is in agreement with the experimental data for the Leucite Hills subbituminous coal shown in Figure III.B-6a. The increase in coal flow rate and steam flow rate causes the location of the maximum temperature to shift toward the bottom of the reactor for the Leucite Hills case. The Utah Blind Canyon case depicted in Figure III.B-6b also shows the effect of increased coal and gas throughputs. Trends in measured and predicted profiles are in agreement. The temperature measurements were taken for two time periods. For the first one, the measurements were repeated on two separate days; but only one set of operational data was reported for this time

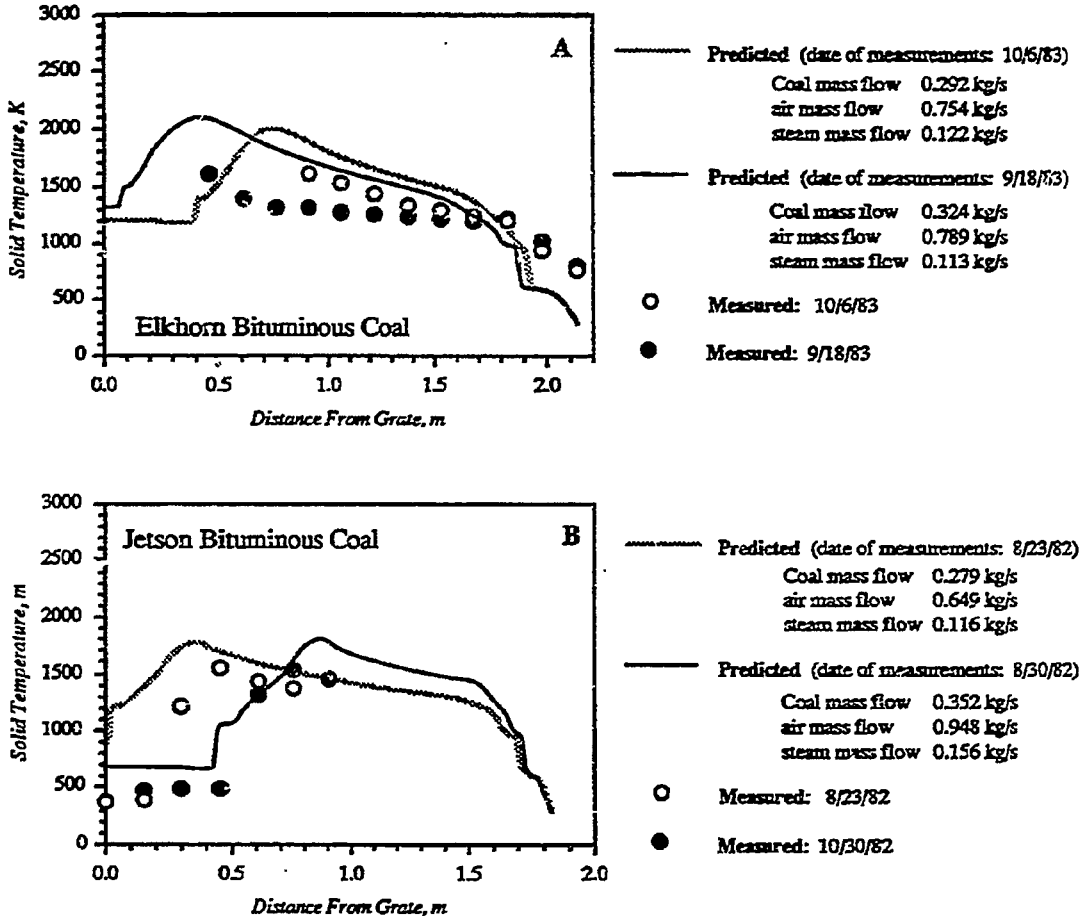

Figure III.B-5 Comparison of measured and predicted solid temperature for several operating conditions for gasification of A) Elkhorn bituminous coal and B) Jetson bituminous coal in an air-fired, low pressure Wellman-Galusha gasifier. Experimental data can be found in Thimsen et al., 1984. Input parameters can be found in Hobbs (1990).

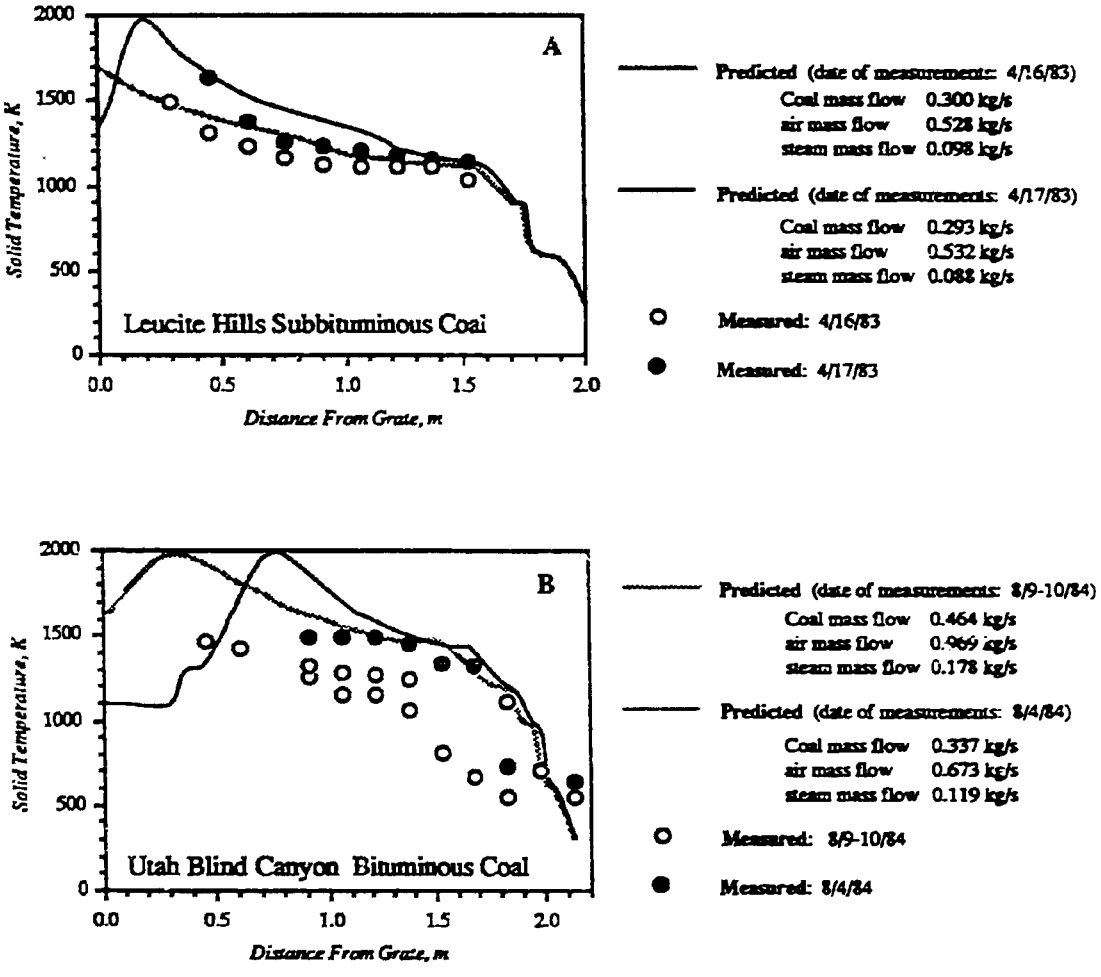

Figure III.B-6 Comparison of measured and predicted solid temperature for several operating conditions for gasification of A) Leucite Hills subbituminous coal and B) Utah Blind Canyon bituminous coal in an air-fired, low pressure Wellman-Galusha gasifier. Experimental data can be found in Thimsen et al., 1984. Input parameters can be found in Hobbs (1990).

period (Thimsen et al., 1984). The spread in experimental data indicates the variability in the experimental data.

Plans

The development of the fixed-bed code will continue next quarter. The two-sigma FG-DVC model will be implemented into the one-dimensional fixed-bed model when available from AFR. Further validation of the one-dimensional fixed-bed model will be necessary after full integration of the FG-DVC submodel. A poster paper entitled "Fixed-Bed Coal Gasification Modeling" will be presented at the 23rd Symposium (International) on Combustion to be held on July 22-27 in Orléans, France.

III.C. SUBTASK 3.C. - GENERALIZED FUELS FEEDSTOCK SUBMODEL

Senior Investigators - B. Scott Brewster and L. Douglas Smoot
Brigham Young University
Provo, UT 84602
(801) 378-6240 and 4326

Objective

The original objective of this subtask was to generalize PCGC-2 to include several types of solid feed, liquid feed and solid-liquid feedstocks. Since there are no submodels being developed in Task 2 that are specifically applicable to liquid-based feedstocks, and since a sulfur/sorbent submodel is being developed under Subtask 2.g, it seemed a more reasonable approach to fulfill the terms of the contract for a generalized feedstocks submodel by generalizing PCGC-2 to include sorbent injection rather than liquid and solid-liquid fuel feedstocks. This approach was outlined in the Phase II Research Plan. An official modification to the work statement for Subtask 3.c was requested from AFR during the last quarter to bring it in line with the above approach.

Accomplishments

Following the approach outlined in the Phase II Plan, work was initiated to extend PCGC-2 to accommodate sorbent injection. The particles will be tracked in a Lagrangian reference frame, similar to the coal. Only one particle size will be allowed. Calcination will be assumed instantaneous, and the CO_2 released during calcination will be added to the carrier gas. Since sorbent particles are small (< 10 μm) and the loading is light, the effect of sorbent on the gas velocity field, temperature, and major gas species will be neglected. Reaction source terms will be provided by the sorbent reactions submodel being developed under Subtask 2.g. The source terms will be used to correct the gas sulfur species concentrations to account for capture by the sorbent.

Plans

Continue modification of PCGC-2 to allow sorbent injection.